Enhancing Joint Communications and Sensing for CubeSat Networks in the Terahertz Band through Orbital Angular Momentum

Sergi Aliaga[a], Ali J. Alqaraghuli[a], Arjun Singh[b], Josep M. Jornet[a]

[a] Northeastern University
805 Columbus Av.
Boston, MA 02115
{aliaga.s, alqaraghuli.a, jmjornet}@northeastern.edu

[b] SUNY Polytechnic Institute
100 Seymour Road
Utica, NY 13502
singha8@sunypoly.edu

Abstract—**This work presents the first space-borne joint communication and sensing (JCS) platform, capable of performing atmospheric humidity sensing while simultaneously transmitting to a Ground Station receiver. Atmospheric sensing is performed through the Differential Absorption Radar approach, which requires transmission at high frequency/high absorption peaks (183 GHz). These frequency requirements are met thanks to the use of state-of-the-art sub-terahertz (THz) frontends, which are also leveraged by the communication system. The proposed design also leverages the latest advancements in wavefront engineering and uses a passive deployeable intelligent reflecting surface (IRS) on board of the satellite to simultaneously combine the communication signals with the sensing signals without interference (orthogonal mode multiplexing). The resulting sytem design performance is evaluated through simulation, achieving up to 400 Gbps and 160 Gbps for output powers of 3 W and 500 mW, respectively.**

TABLE OF CONTENTS

1. INTRODUCTION

With the rise of satellite constellations, advances in wireless communications such as high-throughput space-based Internet are becoming a reality [1]. New telecommunication architectures are even starting to consider the use of CubeSats as part of the 6th-Generation (6G) infrastructure to connect users with high-speed Internet access, leveraging frequencies in the Terahertz (THz) Band (0.1-10THz) which offers large available bandwidth as well as small antennas, capitaliz-

ing on small CubeSat form factors [2]. While this thrust has been fruitful towards terabit-per-second (Tbps) wireless communications, it has raised concerns among the remote sensing community [3]. Here, the highly frequency selective absorption peaks in the THz band have long been utilized to provide Earth Exploration Satellite Services (EESS). Major concerns have been raised about the potential coexistence problem between the remote sensing community and the satellite communications industry for the usage of the yet unlicensed THz portion of the spectrum in space.

Recently, based on enabling high data rate communication [4] as well as high-resolution sensing [5], the concept of joint THz communication and sensing (JCS) in space has been proposed as a candidate solution [6]. In our vision, we see an opportunity to deploy satellite constellations operating in the THz band, enabling space-based cellular and Internet connectivity, while also leveraging the same hardware to perform atmospheric sensing. While such satellites offering dual functionality without relying on separate payloads can reduce real estate and power demands, when designing the payloads the main challenge is that waveforms suitable for communications are often undesirable in sensing, while the waveforms suitable in sensing are often inefficient for communications.

In this paper, we present a CubeSat system design that enables JCS capabilities through a THz communication system and Differential Absorption Radar (DAR), a state-of-the-art THz-based remote sensing technique. The CubeSat further employs an intelligent reflecting surface (IRS) that can be deployed for a highly effective aperture. As shown in Figure 1, the utilization of the IRS allows not only an increase in the gain but a customized wavefront engineering opportunity, through which novel properties of electromagnetic (EM) waves can be exploited [7, 8]. A particular configuration of interest are vortex–beams which carry orbital angular momentum (OAM) [9], whereby signals in the same time, frequency and space channels can be multiplexed and demultiplexed through distinct OAM modes [10]. With such orthogonality guaranteed by the physics of the wavefronts, the design of waveforms for sensing and waveforms for communications can be completely decoupled.

More specifically, in the proposed design, three feed-horns with the same spatial-temporal-frequency channel are utilized

to receive/transmit three signal streams by pointing them towards an IRS onboard the same satellite. The IRS is partitioned into different sections, each of which acts as a passive (no RF chains), programmable reflector that is, effectively, a wave-generating and receiving aperture for and from a particular feed horn, exploiting the time-reversal symmetry of wavefront engineering [11]. The proposed reflector design is based on the recent advances in wavefront engineering, allowing simultaneous transmission of signals incident on each partition within the IRS, with the same frequency and in the same direction, by adjusting their OAM mode order. The mode of order zero (the conventional Gaussian beam) is utilized with a waveform that meets the requirements of DAR, while the rest of modes are reserved for waveforms that maximize the transmission data rate. At the receiver side, the same process is performed in reverse, exploiting the time-reversal symmetry of the design.

The rest of the paper is structured as follows: in Section 2 we introduce the general architecture and operation of the proposed CubeSat design. In Section 3 we provide the technical specifications and operation of both the sensing and communications funcionalities while in Section 4 we detail the design principles of the proposed IRS panel. In Section 5 we evaluate the hardware design limitations imposed by the CubeSat standard form factor and choose the adequate size for the proposed design. In Section 6 we present the simulation results of the proposed design when transmitting to a Ground Station (GS) receiver. Finally, in Section 7 we draw the main conclusions and findings of this study.

2. SYSTEM DESIGN

In this section we break the system design description into a general overview of the system functionalities. The specific technical details that enable each of those functionalities are included in Sections 3 and 4.

The proposed system consists of a CubeSat-standard-compatible satellite designed to transmit information to a ground station receiver while simultaneously acquiring information about the atmospheric conditions at the moment of transmission. Figure1 schematically depicts the satellite shape. Similar to the design in [12], the satellite consists of three feed antenna horns pointing towards a three-fold foldable IRS. Figure 2 schematically describes the system operation and functionalities. Each of the antenna horns point towards one of the three partitions of the IRS, creating three spatially multiplexed channels. Each feed-horn is connected to an adequately designed circulator, which eliminates the need of separate antenna horns for transmission and reception, respectively, essentially minimizing the real-state of the three independent transceivers.

One of the three channels is dedicated to perform remote sensing of the atmosphere humidity. In particular, the satellite uses the Differential Absorption Radar (DAR) concept to retrieve humidity profiles along the beam path, capturing water-vapor density measurements inside clouds, and column-integrated water-vapor measurements in-between cloud layers and the Earth's surface [13]. The operation details of DAR are described in Section 3.

The other two channels are reserved for information transmission to the ground station receiver. Equipped with adjustable bandwidth and adaptive modulation based on the satellites position, each channel leverages state-of-the-art RF
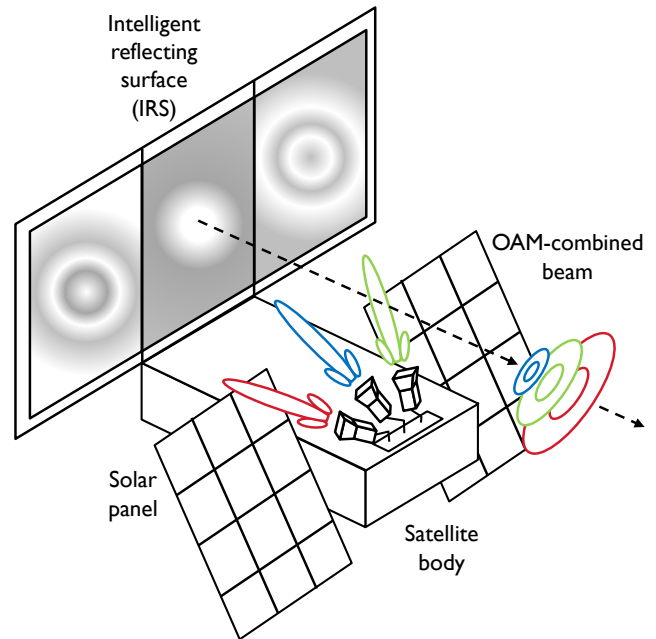

Figure 1: Satellite schematic model after deployment, with multiple feed horns and an intelligent reflecting surface (IRS) that can enable wavefront engineering.

transceivers similar to the ones utilized in the TeraNova testbed at Northeastern University [14], with up to 20 GHz bandwidth allocated in the sub-THz band. As we describe in Section 3, the adjustable bandwidth can be increased when the desired Eb/N_0 can still be met, up to the hardware limitation of 20 GHz. The details of the communication payload operation are specified in Section 3.

The signals from the feed-horn illuminate an intelligent reflecting surface (IRS), which acts as a large aperture device, significantly increasing the beamforming gain. However, in such a setup, we must consider two fundamental limitations: (i) The gain from an aperture has a diminishing return - as the size of the IRS increases, the additional gain increase is not proportional to the corresponding size increase, as shown in Figure 5; (ii) the three independent channels from the three feed-horns are designed to operate at the same frequencies, and thus will interfere with each other [15].

To simultaneously address both these issues, the IRS is partitioned into three subsections, in which each subsection interacts with the signals from a particular feed-horn. Thus, the limited real-estate of the IRS aperture is distributed equally into three partitions, of which two are utilized for communications, and one is utilized for sensing. Further, in addition to providing a beamforming gain, the individual subsections of the IRS are configured to implement a phase transformation matrix on the incident Gaussain beams, infusing them with a distinct Orbital Angular Momentum (OAM). The signal which carries the sensing waveform is left unaltered, whereas the two communication streams are provided with equal, and opposite OAM. Distinct OAM modes exhibit zero spatial cross-correlation with each other - thereby, OAM multiplexing achieves the same increase of data rate as perfect coding gain in uncorrelated MIMO channels.

2
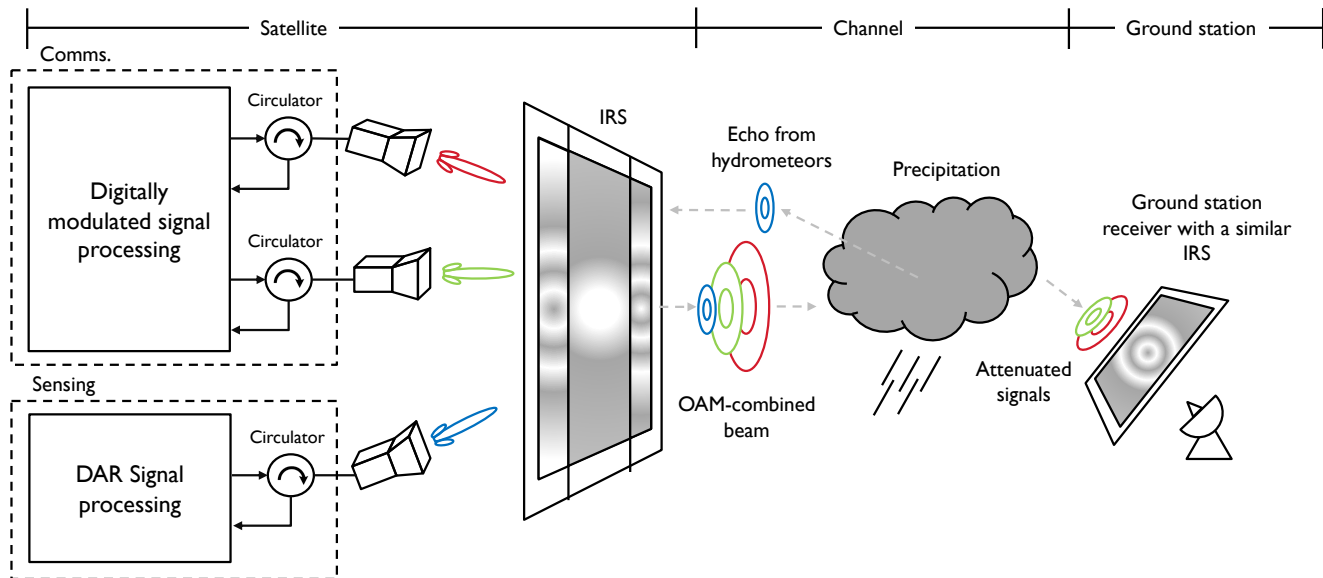
Figure 2: Spaceborne Joint Communication and Sensing system design and operation in transmission. The IRS operation is shown as a phase transformation matrix for visual convenience.

3. SIGNAL GENERATION – WAVEFORMS

Differential Absorption Radar

Differential Absorption Radar (DAR) is a mono-static remote sensing technique used for the acquisition of density measurements at different ranges of the radar (known as the density profile) of any substance in the atmosphere whose molecular composition causes high absorption of electromagnetic waves at a small range of frequencies, or what is known as an absorption peak or line. DAR is the RF reciprocal of Differential Absorption LIDAR (DIAL), which operates at optical frequencies. The main benefit of DAR over DIAL is its profiling capabilities inside clouds, as opposed to DIAL, which is only capable of obtaining density profiles in clear-sky conditions. More specifically, because of their frequency range and corresponding range of wavelengths, signals sent by DAR originate echoes from the hydro-meteors that form clouds and precipitation, while for DIAL signals, the echoes of interest originate from atmospheric aerosols and are completely absorbed in the presence of clouds.

In this work, the substance of interest is the water vapor present in all layers of the atmosphere. DAR enables two distinct measurement capabilities for water vapor: (1) the density profile inside clouds, and (2) the column-integrated water vapor (IWV) between the radar and the first cloud layer, or in-between cloud layers. This last type of measurement is of interest because in the absence of clouds, the only echo received at the radar is the return from the first cloud layer, or the Earth's surface, in case of an airborne DAR platform. In this section we provide some insights on the specific waveform used by DAR to obtain these two measurements and the expressions to measure the performance of the echo acquisition, as well as some background on how the density and IWV measurements are retrieved from the received radar echoes.

In general, two major steps are required to operate DAR: first, reflectivity data, or radar echoes, need to be acquired through the radar system; and, second, two different retrieval methodologies are applied to obtain the density profile measurements and the IWV measurements, respectively.

Radar echo measurements—The radar instrument required to obtain the measurements for DAR basically needs to transmit signals at two separate frequencies alternatively, one as close as possible to a water vapor absorption line, called on-line frequency, and one at a comparably low absorption frequency, either at a higher or lower band, called off-line frequency. The absorption lines of water vapor at frequencies with a wavelength comparable to the size of the hydro-meteors of interest show considerably wide profiles, spanning relative bandwidth of 1-10%, whereas those for DIAL are around 0.01% in comparison. The implementation of a system capable of transmitting two narrow-band signals at two frequencies separated by a fractional bandwidth of 1-10% is extremely challenging. In [5], this is achieved thanks to custom-made front-ends that leverage NASA Jet Propulsion Laboratory (JPL)'s patented multiplier technology based on on-chip power combining [16]. In [5], the water vapor absorption line of interest is the one located at 183 GHz, which is the same one utilized to obtain the results in the present manuscript. However, as explained in [17], due to the ITU spectrum restrictions for the coexistence with passive sensing services, transmission at 183 GHz is not allowed, and the specific frequency utilized is the closest authorized frequency to the absorption peak, i.e., 174.8 GHz. Figure 3 shows the water vapor absorption coefficient around the 183 GHz absorption line, the highest absorption frequency utilized (174.8 GHz), and the maximum operational bandwidth of the state-of-the-art sub-THz frontends.

The primarily quantities obtained by the mono-static instrument are the radar echo powers as a function of range r and frequency f_i for both the online frequency, f_0, and offline frequency, f_1, which are related to the instrument parameters through the standard weather radar equation [20]:

$$P_e(r, f_i) = \frac{Z(r, f_i)e^{-2\tau(r,f_i)}}{C(f_i)r^2} = \frac{Z_{obs}(r, f_i)}{C(f_i)r^2}, \quad (1)$$

3
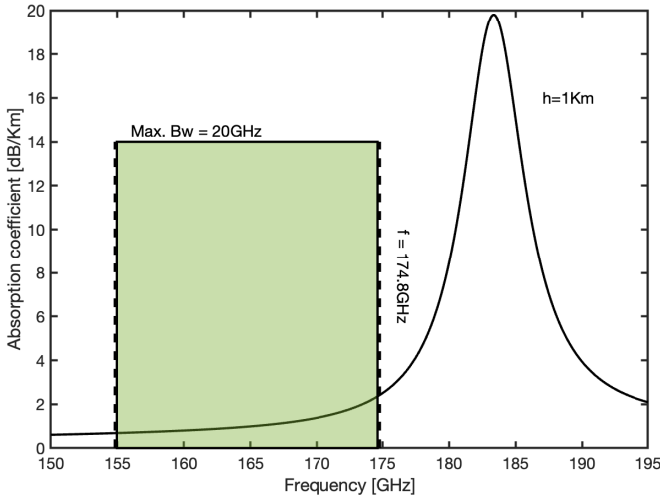
Figure 3: Water vapor absorption coefficient calculated using the ITU Recommendation ITU-R P.676-12 [18] and Recommendation ITU-R P.835 [19]. Highlighted in green is the maximum bandwidth allowable by the state-of-the-art sub-THz frontends in [14]

.

where $Z(r, f_i)$ and $Z_{obs}(r, f_i)$ are the unattenuated and observed reflectivity factors, $\tau(r, f_i)$ is the one-way optical depth from the radar to range r and $C(f)$ is a radar calibration coefficient that captures all the hardware-depending parameters. More details about the calibration of this coefficient are provided in [17]. Although IWV measurements require an accurate calibration of $C(f)$, DAR measurements of density profiles inside clouds are not affected by it since the retrieval involves the ratio of $P_e(r, f_i)$ at two different ranges, effectively cancelling out the calibration coefficient. Therefore, the main source of uncertainty in the retrieved density profiles come from the random error of P_e measurements, as well as the systematic uncertainty related to the frequency-dependent scattering parameters due to the lack of knowledge about the true hydro-meteor Drop Size Distribution (DSD). The systematic uncertainty is futher dicussed in detail in [17]. For the random error, authors in [21] demonstrated that the measurements have a resulting relative error equal to:

$$\frac{\sigma_e}{P_e} = \frac{1}{\sqrt{N_p}} \left(1 + \frac{2}{SNR_{DAR}} + \frac{2}{SNR_{DAR}^2} \right)^{1/2}, \quad (2)$$

where $SNR_{DAR} = P_e(r)/P_n(r)$ is the radar signal-to-noise ratio at range r and N_p is the number of independent pulses incoherently averaged to obtain the echo power measurement. DAR is operated in Frequency-Modulated Continuous Wave (FMCW) mode to increase the transceiver sensitivity compared to a pulsated system. FMCW radars have an explicit mapping between frequency and range, and therefore, we consider the noise power $P_n(r)$ as a function of range.

Density profile retrieval—The standard profile retrieval introduced in [22] begins by combining the echo power measurements to compute the observed extinction coefficient $\beta_{obs}(r, f)$ between two ranges r_1 and $r_2 = r_1 + N_b\Delta r$ as follows:

$$\beta_{obs}(r, f) = \frac{1}{2N_b\Delta r} \ln \left(\frac{Z_{obs}(r_1, f)}{Z_{obs}(r_2, f)} \right), \quad (3)$$

where $r = (r_1 + r_2)/2$, Δr is the range resolution of the radar and N_b is the number of range bins considered. The range resolution of a FMCW radar is related to its bandwidth B as $\Delta r = c/2B_{chirp}$, with c being the speed of light. The observed reflectivity factors are obtained by solving (1):

$$Z_{obs}(r, f) = P_e(r, f)C(f)r^2 \quad (4)$$

The profile retrieval principle for DAR relies on fitting the observed extinction coefficient $\beta_{obs}(r, f)$ to a linear function with respect to the gaseous absorption parameters of water vapor. The fitting function presented in [17, 23], under the assumption of small range increments $N_b\Delta r$, and negligible multiple scattering, is the following:

$$\hat{\beta}_{obs}(r, f_i) = a_1 + a_2(f_i - f_0) + a_3 k_v(r, f_i) + \beta_{g,d}(r, f_i) \quad (5)$$

where it is assumed that measurements are made at the discrete set of frequencies $\{f_i\}$. The quantities $k_v(r, f_i)$ and $\beta_{g,d}(r, f_i)$ correspond to the water vapor absorption cross section and the absorption coefficient for dry air, respectively. As indicated in [17], this parameters can be obtained through other remote sensing methods such as the milimiter-wave propagation model from the EOS Microwave Limb Sounder [24]. The three fitted coefficients $\{a_i\}$ are physically interpreted as follows:

$$
\begin{aligned}
a_1 &\leftrightarrow \alpha(r, f_0) + \beta_h(r, f_0) \\
a_2 &\leftrightarrow \frac{\partial}{\partial f}(\alpha(r, f) + \beta_h(r, f))|_{f=f_0}, \quad (6) \\
a_3 &\leftrightarrow \rho_v(r)
\end{aligned}
$$

where $\alpha(r, f) = (2N_b\Delta r)^{-1} \ln[Z(r_1, f)/Z(r_2, f)]$, $\beta_h(r, f)$ is the hydro-meteor extinction coefficient, $\rho_v(r)$ is the water vapor density at range r and f_0 is a reference frequency within the transmitted band. Clearly, measurements at three or more different frequencies within the operational band are required to fully determine this coefficients. On the one hand, limiting the number of frequencies to the minimum would reduce the overhead dead time during the changes in transmission frequencies. On the other hand, extending the set of transmission frequencies could yield a more precise characterisation of the coefficients. In addition, if the DAR waveform were to be combined with a phase modulation for communications, as in [6], changing the transmission frequency between more than three transmission frequencies could increase security in the link as well as robustness against frequency-dependent fading. In this work, however, we propose the use of a three-frequency approach, since communication will be multiplexed in the independent OAM modes of the wavefront, as explained in Section 4, and the priority then is to maximize the system duty cycle.

Column-integrated water vapor—As detailed in [25], DAR can also estimate the column IWV with the ratio between to surface returns at two different frequencies. The IWV measurement provides information about the water vapor content between the radar and the first reflecting layer encountered by the radar signals. Concretely:

$$IWV = \int_0^r \rho_v(r')dr'. \quad (7)$$

This measurements are of interest for the DAR approach because in the absence of clouds or precipitation, the only

4

echo received is the Earth's surface return or the cloud base after clear sky portions in-between cloud layers. IWV in the absence of hydro-meteor content can also be solved for single-range measurements at two frequencies as:

$$\text{IWV} = \frac{1}{2\langle \Delta k_v \rangle}\left\{\ln\left[\frac{P_e(r,f_1)}{P_e(r,f_2)}\right] + \ln\left[\frac{C(f_1)}{C(f_2)}\right] + \right.$$
$$\left. + \ln\left[\frac{Z(r,f_2)}{Z(r,f_1)}\right]\right\} \tag{8}$$

where:

$$\langle k_v \rangle = \frac{\int_0^r \rho_v(r')\Delta k_v(r')dr'}{\int_0^r \rho_v(r')dr'} \tag{9}$$

and $\Delta k_v(r) = k_v(r,f_2) - k_v(r,f_1)$. (8) reveals the importance of a proper characterisation of $C(f)$ at the two frequencies of interest. The first term in the equation will have an associated random error driven by (2), while the remaining terms may introduce systematic error.

In this work, we characterize the performance of the radar system through the achievable sensitivity for $SNR_{DAR} = 1$, i.e., the minimum detectable reflectivity Z_{min} that can be discerned from noise, at the highest absorption frequency ($f = 174.8GHz$). For that purpose, we utilize the standard radar equation from [20]. Concretely, we incorporate the radar calibration parameter $C(f)$ in (1) and consider that the OAM beam order reserved to DAR corresponds to a Gaussian-shaped antenna pattern:

$$Z_{min}(r,\theta,f) = \frac{1024\ln(2)\lambda^2}{\pi^5 P_{tx}G_{tx}\Delta r|K|^2}r^2 L_{abs}(r,\theta,f) \tag{10}$$
$$kT_{sat}B_{chirp}NF_{DAR}\,SNR_{DAR},$$

where λ is the signal wavelength, P_{tx} and G_{tx} are the transmission power and gain, respectively, T_0 is the antenna temperature of the feed-horn reserved to DAR and F is the noise figure of the satellite's DAR receiver chain. $|K|^2$ is the scattering dielectric constant factor of water vapor molecules, which for this analysis has been assumed to be constant at $|K|^2 = 0.93$ and $L_{abs}(r,\theta,f)$ are the absorption losses according to the ITU Recommendation ITU-R P.676-12 [18] and Recommendation ITU-R P.835 [19].

Communications

Similar to the work presented in [2], we evaluate the performance of the communications system as the highest data-rate achievable by different modulations and their allowable bandwidth given the noise at the receiver. All the quantities in the subsequent analysis are considered to be in dB for a better readability of the derived expressions. Based on the link budget analysis [26], the minimum signal-to-noise ratio at the receiver for a target bit error rate (BER) is:

$$\text{SNR} = 10\log\left(\frac{E_b}{N_0}B_{eff}\right) + NF_{GS} \tag{11}$$

where E_b/N_0 is the energy-per-bit to spectral noise density ratio required to meet a certain BER, B_{eff} is the modulation spectral efficiency given by the chosen modulation order (no coding considered), and NF is the noise figure at the GS receiver. The amount of bandwidth B used represents a trade-off, as it both determines the system's total noise and the

achievable data rate. The maximum noise power N tolerable by the system is given by:

$$N = P_{tx} + G_{tx} + G_{rx} - L - \text{SNR} \tag{12}$$

where P_{tx} is the transmitt power, G is the antenna gain and $L = L_{abs} + L_{spr}$ are the total losses caused by atmospheric absorption L_{abs} and free-space spreading L_{spr}, whose computation is detailed in [2]. The maximum allowable bandwidth B will therefore be:

$$B = \frac{10^{N/10}}{kT_{GS}} \tag{13}$$

where k is the Boltzman constant and T_{GS} corresponds to the system noise temperature at the GS. If the allowable bandwidth is larger than the maximum operational bandwidth of the sate-of-the-art sub-THz front ends [14], i.e. 20 GHz, that maximum is adopted.

Finally, the approximate data rate, without considering any pulse-shaping filter, is obtained as:

$$R = B \cdot B_e ff \tag{14}$$

4. SIGNAL PROPAGATION – WAVEFRONTS

While the modulation order of the signal and the resultant waveform informs about the information carried by the signal, the propagation of the signal is understood through wavefronts, which describe how the signal propagates. More specifically, the wavefront is the locus of points for which the radiated signal has constant phase. Thus, by following the wavefront, we can correctly capture the entire facets of beam propagation, shape and peculiarity.

The signals generated across the feed-horns are radiated and manipulated by the partitioned IRS, wherein each section of the IRS acts independently to configure one particular signal. First, we explain the operation of the individual parition of the IRS that only interfaces with one signal, and then we explain the motivation behind incorporating OAM for improved multiplexing gains with the total unit.

IRS Operation

The IRS acts as a passive array of radiating elements that is utilized for engineering the propagation of the signal by manipulating its wavefront. More specifically, wavefront engineering tells us that wave propagation from a given distribution of sources can be characterized by a superposition of the EM waves from the individual radiating elements.

The IRS shown in Figure 4 a) can intercept an incident wave and transcribe a desired wavefront on it, through a phased codebook. Thus, effectively, the IRS acts as a phase transformation device. Considering a beam traveling in the z-direction, and an IRS in the $x - y$ plane, the definition of a phase transformation matrix across the IRS aperture is given as per the Huygens-Fresnel model [27]. Here, EM scalar diffraction theory is utilized to evaluate the complex amplitude $A(x,y,z)$ of the EM wave with a wavevector k at any point from a given field distribution $A(\xi,\eta,0)$ at an aperture (ξ,η) orthogonal to the wave propagation direction z [28]:

$$A(x,y,z) = \frac{1}{j\lambda}\iint_S A(\xi,\eta,0)\frac{\exp(-jkr_1)(1+cos\psi)}{2r_1}d\xi\,d\eta. \tag{15}$$

In (15), $cos\psi$ and r_1 both specify the information about the orientation and distance of the point (x,y,z) from the
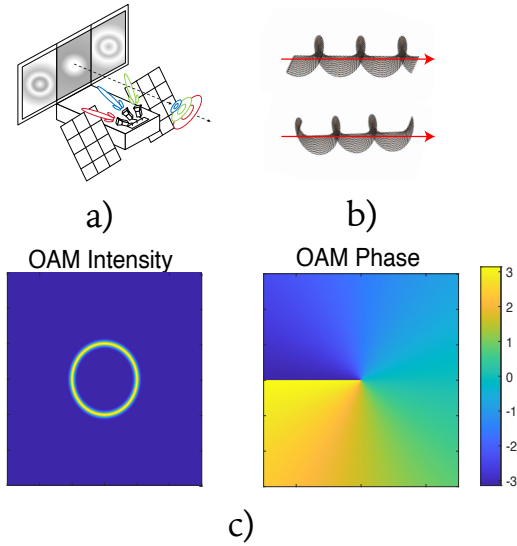
Figure 4: Working principle of the IRS: a) The IRS onboard the CubeSat can intercept a Gaussian wave and convert it into a different OAM carrying Laguerre-Gaussian (LG) beam, with a helical path as shown in b) OAM helical path of $l = 1$ (top) and $l = -1$ (bottom), where the arrows shows the direction of propagation. The phase singularity is generated through a spiral phase with an annular intensity of the resulting beam as shown in; c) the intensity and phase of the beam in the tranverse direction for an $l = 1$ OAM mode. The color bar represents the phase in radians.

aperture spot (ξ, η). The complex field $A(\xi, \eta, 0)$ is given as $\S \exp(j\Phi)$, where $\S$ is the magnitude and Φ is the phase through which the IRS response manifests within the resultant complex field in (15).

The well known beamforming principle of arrays simplifies this complex field evaluation into the simple principles of gain and beamwidth. More specifically, an aperture size of the IRS directly relates to a beamforming gain, in which the wavefront is supposed to have a divergence, or a spreading out factor, as reduced as possible. The linear gain G_{lx} of a device with an aperture of A at a design wavelength of λ is:

$$G_{lx} = \frac{4\pi A}{\lambda^2}, \qquad (16)$$

which reduces the beamwidth of the radiated beam by increasing the directivity. Assuming the directivity equal to the gain, the solid radiation angle Ω, is found as:

$$\Omega = \frac{\pi^2}{G_{lx}}, \qquad (17)$$

which governs how tightly focused the beam is in 3-D space. The gain helps to increase the SNR, which can be utilized to increase the capacity of a system.

Increasing the capacity

The capacity C of a wireless channel is proportional to the utilized bandwidth B, the spatial reuse or diversity factor K, the spectral efficiency B_{eff} and the users signal to noise ratio SNR,

$$C \propto K \cdot B \cdot B_{eff} \cdot \log_2(1 + SNR). \qquad (18)$$

It is critical to note that an increase in the SNR increases the capacity only at a logarithmic scale, and an ever-increasing

size brings diminishing returns in increasing the gain, and therefore, the recovered SNR. Thus, simply trying to maximize the gain by increasing the IRS area produces a logarithmic increase in SNR, and further increases in SNR bring a logarithmic increase in the system capacity - an inefficient design beyond the minimum threshold SNR required for good throughput. As an alternative, spatial reuse and diversity K, whic would bring a linear increase in capacity, can be achieved by using, for example, MIMO techniques, which allow multiple data streams to be transmitted over the same time and frequency resources.

The same strategy can be extended in our system, by partitioning the IRS into smaller units, each of which are served by a feed-horn with an independent RF-chain, and thus increase the system capacity through effective spatial multiplexing. However, in such a setup, given the confined spacing of the feed-horns and the antenna elements, the long distances of communication, it is clear that the channels will not be uncorrelated, significantly penalizing the SNR term, and reducing the effective increase. The problem is further increased as the signals utilized for sensing could be easily corrupted by this interference from the signals utilized for communications, rendering one of the mission requirements defunct. To greatly increase the independence of multiple channels without sacrificing gain, bandwidth or spatial domains, we exploit another property of certain wavefronts: their Orbital Angular Momentum.

Orbital Angular Momentum (OAM)

Certain wavefronts possess new properties which open the door to new communication strategies. The most widely researched and explored among these is OAM, a property of light first demonstrated by Allen et al. [9]. Specifically, a beam that is said to have OAM manifests a spiral phase in the transverse direction, resulting in a helical wavefront and a phase singularity (a zero-intensity vortex) in the center, as shown in Figure 4 b). Such beams require a spiral phase $exp(jl\theta)$, where θ is the transverse azimuthal angle and l specifies the topological charge, or the mode, of the OAM within the beam. The helical wavefront suggests that the wave has a a twisted propagation path, with a central phase singularity. Thus, the intensity of such a beam can be expected to look like an annular ring, or donut shaped, as seen in Figure 4 c). The summary of nearly four decades of research on these beams is presented in [29].

There are multiple ways to generate these beams, all of which involve applying a spiral phase to a regular Gaussian beam. For example, spiral phase plates [10, 29–31], travelling wave antennas [32], and circular antenna arrays [33–35] all produce OAM beams by applying a progressive phase difference ϕ, which in the case of circular arrays composed of N elements, can be expressed as:

$$\phi = 2\pi l/N, \qquad (19)$$

where l is the desired mode of the resultant beam. In such a manner, the regular Gaussian beam is converted to a Laguerre-Gaussian (LG), with the amplitude distribution of the LG_l beam with mode l given as [36]:

$$LG_l(r, \theta, z) = A(r, z, p)exp(jl\theta), \qquad (20)$$

wherein the field distribution $A(r, z, p)$ characterizes the Gaussian propagation in cylindrical coordinates and also includes the manifestation of the radial index p. While the radial index p is also gaining attention as another property

of light which maybe be manipulated, for the time being, we focus on the azimuthal index l. It is vital to observe that the application of $l = 0$, exhibiting the absence of a topological charge points back to the regular Gaussian beam (regular beamforming). Thus, the design and propagation aspects of the previous sections with regard to beamforming gain are equally valid for beams with different OAM modes as well; larger arrays create a more focused OAM beam, with reduced divergence, or spreading.

An integer value of this topological charge l denotes an OAM beam as 'pure'. Pure OAM modes are orthogonal to each other, exhibiting zero cross-talk (interference) amongst each other in theory. More specifically, the correlation between two OAM beams, each with a different topological charge, can be given as:

$$\int_0^{2\pi} exp(jl_1\theta)exp(jl_2\theta)^* d\theta = \begin{cases} 0 & l_1 \neq l_2 \\ 2\pi & l_1 = l_2 \end{cases}, \quad (21)$$

which indicates that different modes can be assigned to different data streams and propagate within the same channel (frequency, time and space) without observed interference, adding another layer of exploitation and thus greatly increasing the system capacity [37].

The benefits of LG-OAM mode multiplexing have been shown in both the optical and the millimeter wave domain. In fact, for a given antenna array size, it is seen that the capacity from OAM communications is same as that of classical uncorrelated MIMO [38]. However, as shown in [39], OAM based mode division multiplexing offers a simpler receiver structure and higher capacity than point to point MIMO [31], especially when MIMO systems are not completely uncorrelated, as we have already explained would happen in our system.

Although theoretically the number of OAM modes is infinite, we have certain restrictions in finite array systems, which we expand upon in more detail in Section 5. We next explain how the individual IRS partitions are globally co-ordinated for an effective OAM-multiplexed system.

General IRS operation

We reserve the $l = 0$ mode order for the sensing application, leaving it unchanged. We further utilize two more partitions, which are configured to generate the $l = 1$ and $l = -1$ modes, for the two communication streams. Beams with distinct OAM modes are always orthogonal to each other, and the resulting cross-correlation is guaranteed to be zero. Therefore, the three multiplexed streams, with $l = 1, 0, -1$ can exist simultaneously.

At the receiver side, a similarly designed IRS is utilized to demultiplex the OAM beams. More specifically, similar to [40–42], the RX_{IRS} implements the required phase, as per (20), such that only the correct signal is made available at the correct feed-horn of the receiver. Thus, the RX acts as a specialized diffraction grating, which diffracts an incident beam to a particular focal spot only when the mode order is correct. Consider an LG-OAM beam incident on an IRS in which a specialized diffraction grating is applied. Thus, the IRS varies a number of diffraction grating spots $A(l_{max})$, with modes $l \in [-l_{max}, l_{max}]$. The beam incident on such an IRS is diffracted to the specific spot when the mode of the beam is cancelled by the mode of that particular diffraction grating order. Since the incident beam had a donut intensity with a spiral phase, the diffracted beam has a planar wave-

front, with an annular ring-like intensity. By applying the spatial Fourier on this zero-order annular ring, a zero-order Bessel with a high peak intensity in the centre is obtained at the specific diffraction spot, which can then be recovered by the feed horn at that point.

5. HARDWARE DESIGN AND LIMITATIONS

From a hardware standpoint, the main hurdle in developing terahertz communication systems has been the lack of efficient sources. This has been mainly hindered by the lack of available oscillators at terahertz frequencies. Thus, the only two options for generating terahertz signals has been either through up-conversion from microwaves, or down-conversion from RF photonics [4]. Indeed, with the use of frequency multipliers, terahertz signals can be up converted from microwave oscillators, and certain configurations have been developed by multiple groups such as Virginia Diodes [43] and the NASA Jet Propulsion Laboratory [44], and such upconversion methods prove to result in higher transmit powers than RF photonics mehtods, and thus are more likely to be considered for terahertz applications. Nonetheless, challenges in developing end-to-end RF chains at terahertz frequencies limit the possibilities of feeding multi-pixel antenna arrays such as phased-arrays, and thus crown conventional horns as the current traditional terahertz antennas due to passivity and and ease of manufacturing. In this section, we propose a realistic architecture based on existing terahertz technology, and present passive reflect arrays as the optimal candidate for enhancing terahertz signals with higher gain and for manipulating wave fronts to increase data rates.
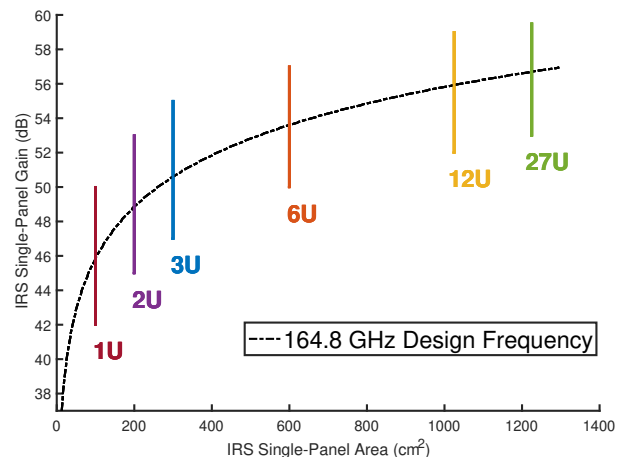
Figure 5: IRS gain as a function of a single panel area. Vertical lines indicate the total deployed size of the IRS for different CubeSat standard form factors. The exact gain values are included in Table 1

.

RF Chains

The envisioned terahertz hardware chain is composed of an all-electronic monolithic millimeter wave integrated circuits (MMIC) based on high-electron-mobility transistors such as GaAN or InGaAs, as developed in [44]. Such technologies have been used for spectroscopy and radar applications, as well as showing communication demonstrations above 100 GHz. Furthermore, compact terahertz devices are suitable for CubeSat applications, given their reduced size and power consumption and do not require cryogenic cooling, unlike other technologies such as quantum-cascade lasers [4]

CubeSat Configuration	Weight (kg)	Size (cm x cm x cm)	IRS Aperture (cm^2)	Single-Panel Gain (dBi)
1U	1.33	10 x 10 x 10	300	45
2U	2.66	10 x 10 x 20	600	48
3U	3.99	10 x 10 x 30	900	51
6U	7.98	10 x 20 x 30	1800	54
12U	15.96	20 x 30 x 35	3150	56
27U	35.91	30 x 35 x 35	3675	57

Table 1: A list of CubeSat configurations based on size, weight, and aperture area of the 3-panel configuration.

. To implement a terahertz active radar in combination with ultrabroadband communication, similar building blocks can be implemented based on superheterodyne schottky-diode-based terahertz sources as found in [5]. The key components include high-power terahertz sources at the transmitter and low-noise broadband mixers at the receiver, with key metrics such as source power and stability at the transmitter, as well as mixer conversion loss and noise temperature at the receiver [4]. In the past decade, various demonstrations showed high-power frequency-multiplied sources based on patented power-combining Gallium Arsenide Schottky diode technology, with ranges starting in the G-band as desired in this paper, in addition to low-noise broadband mixers based on same technology. A preliminary block diagram of the proposed hardware architecture is depicted in Figure 6, showing three separate channels, with two channels serving for broadband communication while one channel is reserved for atmospheric sensing. Finally, each RF chain ends with a feed-horn antenna pointing at the intelligent reflecting surface as shown in Figure 2.
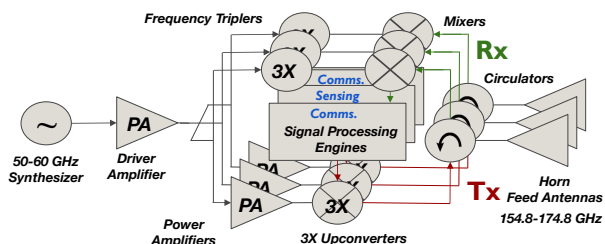
Figure 6: A block diagram of the hardware configuration for the three channels, encompassing transmission and reception with joint communications and sensing controls through a shared narrowband/wideband signal processing unit.

IRS Design and Operating Considerations

The design criterion of the IRS are limited by the size of the CubeSats. More specifically, as we explain in Section 6, for a given CubeSat size, the antenna aperture is generally limited to the size of the larger side in the CubeSat, such as the CubeSat antenna demonstrated in [45]. Nonetheless, recent advancements in CubeSat antennas such as NASA Mars Cube One satellite have demonstrated foldable, deployable reflecatarrays in space in the Martian orbit [12]. The main design revolved around folding three separate antenna panels, each sized as the larger side of the CubeSat, and using hinges alongside a mechanical deployment mechanism to expand the size of the IRS in orbit. However, beyond a certain aperture length, the increase in gain with respect to the increase in aperture size decreases significantly. In our design, the folded three-panel IRS is adopted with the novelty that one panel has passive sensing, while using the two other panels for communication, each occupying a standalone OAM mode.

Since the IRS does not have any active RF chains, there is no limitation of feed lines that restrict the size envisioned. Thus, while the size of the IRS can be increased substantially, a key requirement is the design strategy. On the one hand, the IRS can be designed through an antenna array technique, similar to [7], in which the elements are spaced apart by $\lambda/2$. Such an IRS constitutes individual radiating elements on the order of the design wavelength and can be operated through the principles of beamforming where each element has no mutual coupling with the other and the phased array response can be calculated as a codebook application. On the other hand, similar to [8, 46], a metasurface-based IRS can be designed, in which tightly packed sub-wavelength-sized elements have a mutually coupled radiation response. The metasurface-based strategy allows for a more precise phase transformation matrix, since there is a denser number of elements within the same aperture, but lacks a clear-cut methodology to generate the desired wavefront response; metasurface designs cannot be repurposed to different design frequencies and bandwidths as hardware improves.

However, the IRS is not required to steer the beam, and thus a dynamic phase shifter is not required. The entire operation of the IRS can be pre-configured before deployment, and for steering purposes, mechanical steering of the CubeSat feature can be explored, as in [45, 47]. Thus, a metasurface-based design is more appealing, as that provides a greater density of the aperture [8], and thus the generated modes from the array can be guaranteed to be pure [35]. In our design, we rely on a fixed horn and a fixed IRS, with the mechanical steering mechanism falling under the altitude determination and control subsystem which directly determines the satellite's orientation at all times.

OAM Modes - Benefits and Limitations

Benefits—A point worth considering is if the two partitioned sections utilized for multiplexing communications waveforms through two different OAM modes were to be joined and utilized for a single data stream, which it appears as though an additional 3 dB of SNR would be present. Following the discussion from equations (11) - (13), this would increase the noise tolerance, thus increasing the allowable bandwidth, and the data rate would significantly improve. Even in the case that the entire bandwidth allowed by the hardware is used (20 GHz), a larger SNR allows higher-order modulations to be utilized, thus increasing the spectral efficiency.

At the same time, it is important to realize that for beamforming gain, the elements of the IRS realize a parabolic, lens-like collimating phase in addition to the OAM-generating spiral phase on the EM radiation. Clearly, the same design optimizations as in a parabolic mirror are then valid. As explained in detail in chapter 15 of [15], as the diameter of the aperture increases, the focus (where the feed-horn should be placed) should also be spaced further from the aperture.

8

Thus, for such two times larger aperture supporting a single data stream, and operating with the same efficiency, the size of the cube-sat would have to be significantly increased to accommodate the feed-horn to the corresponding focal-point. If, instead, the size of the cube-sat is not increased, then, following the discussion from figure 15.10 in [15], the efficiency would decrease by almost 50%, effectively countering the theoretical 3 dB increase in gain. Clearly, the exploitation of OAM provides an easy method to best utilize a large aperture, without involving complex signal processing, and guaranteeing orthogonality.

Limitations— As described in Section 4, we utilize three OAM modes, in which OAM of mode $l = 0$ is the regular Gaussian, utilized for sensing, and OAM modes $l = 1, -1$ are utilized for communications. The natural question is then what prohibits the utilization of more OAM modes, to increase the multiplexing capability? Indeed, if the present IRS was to be partitioned into even two smaller units, then we could have 4 OAM modes, with an SNR penalty of only 3 dB. However, as shown in [48], as the OAM mode increases, the divergence, or the spreading increases. Thus, higher-order OAM modes require larger arrays for generation, which is a non-trivial design task. In addition, as the intensity profile of OAM carrying wavefronts is annular, there exists an intensity null in the center, with the power distributed in the region surrounding that null. Therefore, if the divergence is too great, especially when the size of the communication distance is as large as in a satellite communications scenario, the utilization of higher mode order OAM beams can be detrimental to the overall system design goal – improved communications. To this end, we restrict ourselves to OAM mode order of -1 and 1, with identical divergence, that can be propagated for longer distances.

6. RESULTS

The system parameters considered for the simulation results are summarised in Table 2 [49], and Figure 7 schematically depicts the scenario considered, for clarification purposes, where θ corresponds to the satellite elevation angle towards the GS when passing directly above it (best case scenario).
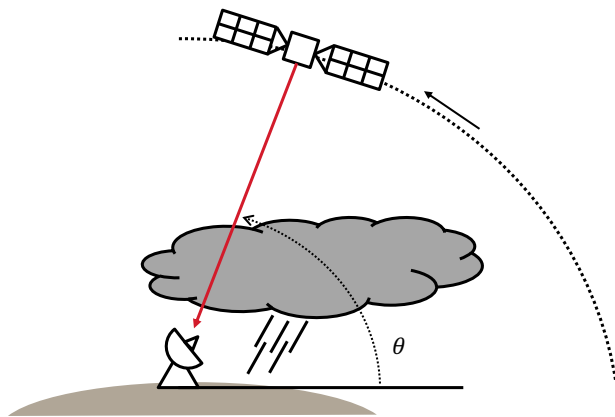
Figure 7: Schematic of the scenario considered. θ corresponds to the satellite elevation angle towards the GS.

DAR Performance and Sensitivity

The results shown in Figure 8 depict the achievable radar sensitivity as a function of the satellite elevation angle for dif-

ferent ranges, considering the satellite altitude $h = 400 Km$. As expected, the sensitivity is constant for all elevation angles until the beam enters the atmosphere, that is, for ranges $r > 300\ Km$ or, equivalently, $h < 100\ Km$. At these altitudes, especially at the lowest layers of the atmosphere, the water vapor absorption deteriorates the radar signal and increases its sensitivity. This performance reduction is especially noticeable at low elevation angles, since the beam has to traverse longer slant paths through the atmosphere. Furthermore, the weather conditions above the ground station could increase even more the detectable sensitivity of the radar in the presence of precipitation or high concentration of absorbing substances. Therefore, further development of the DAR concept for space-borne platforms is required to provide the satellite with more robust sensing capabilities.

General	
Altitude, h	400 km
Transmitted power per channel, P_{tx}	3 W / 500 mW
Transmitter antenna gain, G_{tx}	56 dB
Noise figure, F	8 dB
Communications	
BER	10^{-7}
GS antenna gain , G_{rx}	58 dB
GS system noise temperature, T_{GS}	100 K
GS Noise figure , NF	7 dB [*]
Center frequency	164.8 GHz
Max. allowable bandwidth	20 GHz
Sensing	
Highest absorption transmit frequency f	174.8 GHz
Bandwidth, B_{chirp}	60 MHz
Range resolution, Δr	15 m
Dielectric constant, $|K|^2$	0.93
Receiver noise temperature, T_{sat}	290 K
Receiver Noise figure , NF_{sat}	7 dB [*]
Number of pulses , N_p	2000
Relative random error, from (2)	5%

[*] Typical value for state-of-the-art THz receivers [49].

Table 2: System parameters

Improvements to Communications With OAM

We show in Figure 9 the results for the communication link performance as the total data rate achievable at the different stages of the communication link, i.e. as a function of the elevation angle, and for different modulation orders (considering QAM modulations). From the link budget ((13)), we computed the necessary power that grant a high enough SNR to utilize the maximum bandwidth allowed by the sub-THz front ends (20 GHz) at zenith, which is around 3 W. From Figure9a, it can be seen that the system is able to reach a data-rate of 400 Gbps at zenith and with the highest modulation order, several orders of magnitude above what current satellite operators can offer. This is achieved thanks to the multiplexing of the two communication streams with the two IRS panels not used for DAR. For comparison, we studied the data rate achievable when the exact same two panels are combined together and used by a single communication stream (i.e. no OAM multiplexing). In this case, as explained in section 5, the gain provided by the IRS is affected in two ways, compared to using a single panel for
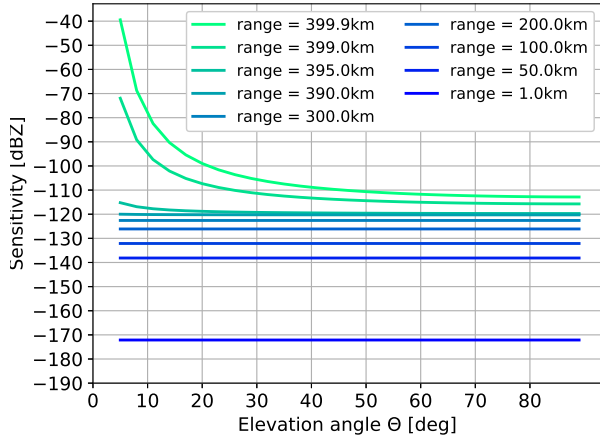
Figure 8: Radar sensitivity for a threshold $SNR_{sat,th} = 1dB$ at different ranges and elevation angles.

each communication stream: (1) doubling the aperture area results in a 3 dB increase approximately, and (2) there is a reduction in the antenna efficiency from 0.83 to 0.45, which results into a 2.66 dB reduction in gain [15]. As explained, this reduction in efficiency is caused by the fact that, with this larger antenna aperture, the feed-horn would no longer be located in the focal point of the reflector. To locate the feed-horn to the new focal point, it would require to move the horn further away from the reflector, essentially requiring an increase in the dimensions of the satellite. In Figure 9b we include the communication link performance in this scenario, when no OAM is considered. It can be observed that the resulting datarates would be reduced considerably, up to a half at high elevation angles, when the transmitter can utilize the entire bandwidth of the system.

Despite these promising results, we acknowledge that at this moment in time, it is not only hard to find a CubeSat battery large enough to provide the required power to achieve such high speeds, but neither the state-of-the-art THz sources can support it. For this reason, we additionally include the results of the communication link when the current state-of-the-art is considered, in Figure 9c and 9d, respectively. In this scenario, a total output power of 500 mW is considered, which is the present state-of-the-art at 180 GHz [44]. The results show that, for now, an OAM-enhanced system would be able to achieve a total data rate of 160 Gbps, which is still higher than most of current systems, while the rate achieved without wavefront engineering would again be reduced by almost a half. We believe this shows a clear motivation to push the state-of-the-art to continue increasing the maximum radiated power at THz and sub-THz frequencies, and it is only a matter of time until it gets there. One thing to notice is that in the high output power case, the maximum rate is achieved by the high order modulations, whereas in the lower power scenario, it is the lower order modulations that achieve the highest data rate. This is due to the fact that when a higher power is available, for a fixed SNR requirement, i.e., fixed BER, the system noise tolerance is larger and, therefore, the maximum allowable bandwidth is also higher. In that case, the bandwidth is not limited by the tolerable noise but rather by the hardware limitations (20 GHz). For this reason, when the bandwidth reaches the 20 GHz limit for all modulations, higher order modulations exploit better the spectrum portion thanks to higher bandwidth efficiencies. On the other hand, in power restricted scenarios, the maximum allowable bandwidth is limited by the tolerable noise, which is higher in lower order modulations. For this reason, lower order modulations perform better in power-limited scenarios.

7. CONCLUSION

In this paper we propose the first CubeSat design capable of performing atmospheric humidity sensing while providing unprecedented downlink throughput, all at the same time and band, effectively proposing the first Spaceborne Joint Communication and Sensing platform. We achieve the presented functionalities by leveraging three main technologies: (1) state-of-the-art sub-THz front-ends leveraging NASA Jet Propulsion Laboratory (JPL)'s patented multiplier technology based on on-chip power combining, (2) Differential Absorption Radar for water vapor density profile retrieval and Column-Integrated Water Vapor measurements, and (3) state-of-the-art IRS designs able to perform wavefront engineering and leverage the Orbital Angular Momentum of EM waves. The results show that data rates up to 400 Gbps will be achievable when new THz sources and antenna design milestones are met, and that current technology would be able to achieve a total throughput of 160 Gbps. The addition of sensing capabilities to such new generation of High-Throughput Satellites combined with multi-satellite architectures (constellations) could trigger the deployment of satellite systems that not only would bridge the current digital divide but would also sample atmospheric data at a scale never seen before, hopefully helping the research community to better understand our planet's climate evolution.

REFERENCES

[1] N. Pachler, I. del Portillo, E. F. Crawley, and B. G. Cameron, "An updated comparison of four low earth orbit satellite constellation systems to provide global broadband," in *IEEE International Workshop*, 2021.

[2] A. J. Alqaraghuli, H. Abdellatif, and J. M. Jornet, "Performance analysis of a dual terahertz/ka band communication system for satellite mega-constellations," in *2021 IEEE 22nd International Symposium on a World of Wireless, Mobile and Multimedia Networks (WoW-MoM)*, Jun 2021, p. 316–322.

[3] I. Levchenko, S. Xu, Y.-L. Wu, and K. Bazaka, "Hopes and concerns for astronomy of satellite constellations," *Nature Astronomy*, vol. 4, no. 11, pp. 1012–1014, 2020.

[4] I. Mehdi, J. Siles, C. P. Chen, and J. M. Jornet, "Thz technology for space communications," in *2018 Asia-Pacific Microwave Conference (APMC)*. IEEE, 2018, pp. 76–78.

[5] K. B. Cooper, R. J. Roy, R. Dengler, R. R. Monje, M. Alonso-Delpino, J. V. Siles, O. Yurduseven, C. Parashare, L. Millán, and M. Lebsock, "G-band radar for humidity and cloud remote sensing," *IEEE Transactions on Geoscience and Remote Sensing*, vol. 59, no. 2, p. 1106–1117, Feb 2021.
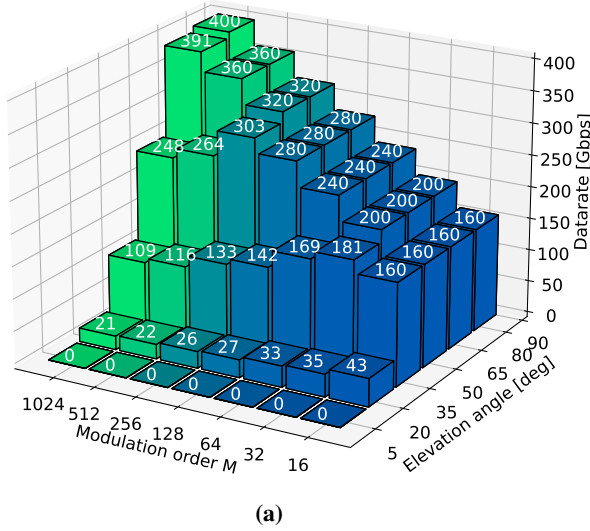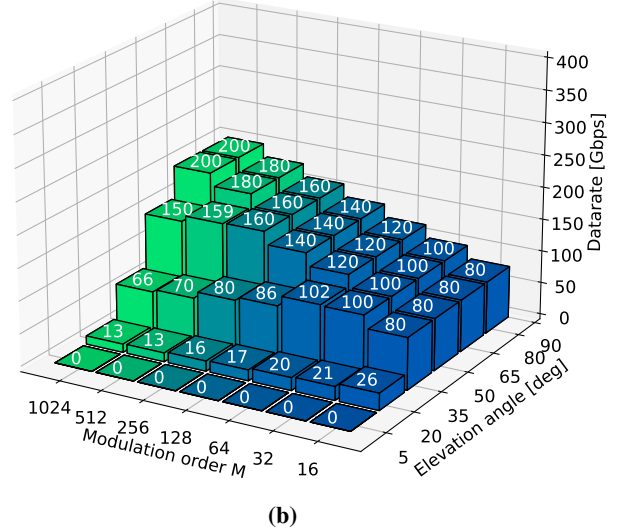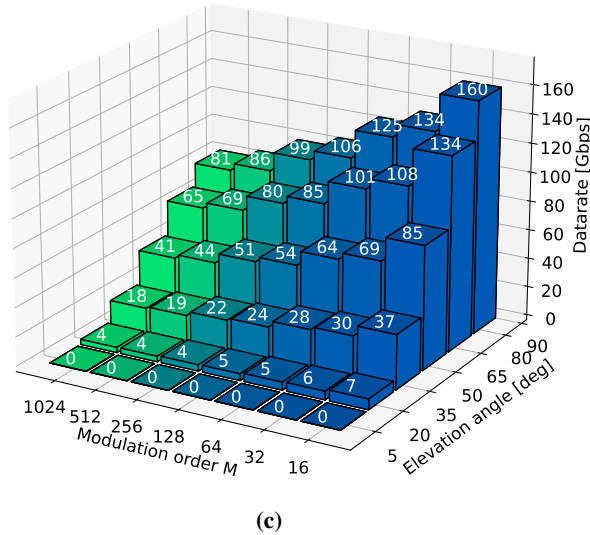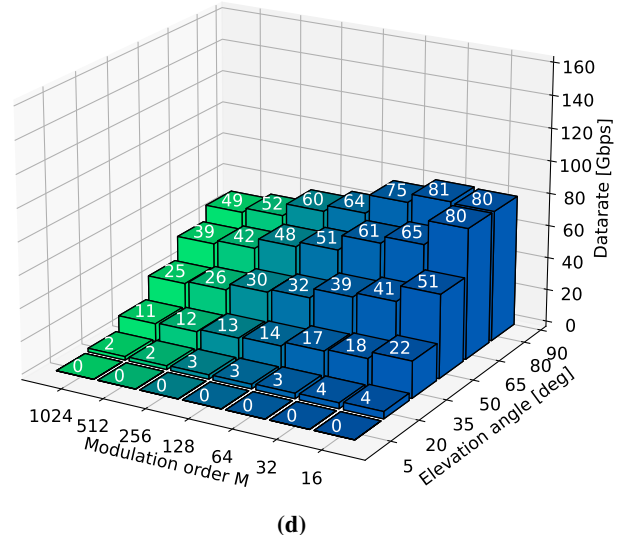
Figure 9: Communication link performance as a function of the satellites position above the GS (elevation angle) for different QAM modulation orders. OAM modes = 1 refers to the case in which the whole IRS is used for communications and no sensing is enabled.

[6] S. Aliaga, A. J. Alqaraghuli, and J. M. Jornet, "Joint terahertz communication and atmospheric sensing in low earth orbit satellite networks: Physical layer design," in *2022 IEEE 23rd International Symposium on a World of Wireless, Mobile and Multimedia Networks (WoWMoM)*, 2022, pp. 457–463.

[7] A. Singh, M. Andrello, E. Einarsson, N. Thawdar, and J. M. Jornet, "A hybrid intelligent reflecting surface with graphene-based control elements for THz communications," in *2020 IEEE 21st International Workshop on Signal Processing Advances in Wireless Communications (SPAWC)*. IEEE, 2020, pp. 1–5.

[8] C. Liaskos, S. Nie, A. Tsioliaridou, A. Pitsillides, S. Ioannidis, and I. Akyildiz, "A novel communication paradigm for high capacity and security via programmable indoor wireless environments in next gener-

ation wireless systems," *Ad Hoc Networks*, vol. 87, pp. 1–16, 2019.

[9] L. Allen, M. W. Beijersbergen, R. Spreeuw, and J. Woerdman, "Orbital angular momentum of light and the transformation of laguerre-gaussian laser modes," *Physical review A*, vol. 45, no. 11, p. 8185, 1992.

[10] Y. Yan, G. Xie, M. P. Lavery, H. Huang, N. Ahmed, C. Bao, Y. Ren, Y. Cao, L. Li, Z. Zhao *et al.*, "High-capacity millimetre-wave communications with orbital angular momentum multiplexing," *Nature communications*, vol. 5, no. 1, pp. 1–9, 2014.

[11] D. L. Sounas and A. Alu, "Time-reversal symmetry bounds on the electromagnetic response of asymmetric structures," *Physical review letters*, vol. 118, no. 15, p. 154302, 2017.

[12] R. E. Hodges, N. Chahat, D. J. Hoppe, and J. D.

Vacchione, "A deployable high-gain antenna bound for mars: Developing a new folded-panel reflectarray for the first cubesat mission to mars." *IEEE Antennas and Propagation Magazine*, vol. 59, no. 2, p. 39–49, Apr 2017.

[13] L. Millán, M. Lebsock, N. Livesey, and S. Tanelli, "Differential absorption radar techniques: water vapor retrievals," *Atmospheric Measurement Techniques*, vol. 9, no. 6, p. 2633–2646, Jun 2016.

[14] P. Sen, V. Ariyarathna, A. Madanayake, and J. M. Jornet, "A versatile experimental testbed for ultrabroad-band communication networks above 100 ghz," *Computer Networks*, vol. 193, p. 108092, Jul 2021.

[15] C. A. Balanis, *Antenna theory: analysis and design*. John wiley & sons, 2016.

[16] J. V. S. Perez, G. Chattopadhyay, C. Lee, E. T. Schlecht, C. D. Jung-Kubiak, and I. Mehdi, "On-chip power-combining for high-power schottky diode based frequency multipliers," Sep 2015. [Online]. Available: https://patents.google.com/patent/US9143084B2/en

[17] R. J. Roy, M. Lebsock, L. Millán, and K. B. Cooper, "Validation of a g-band differential absorption cloud radar for humidity remote sensing," *Journal of Atmospheric and Oceanic Technology*, vol. 37, no. 6, p. 1085–1102, Jun 2020.

[18] "Attenuation by atmospheric gases and related effects," *International Telecommunication Union*, vol. P.676-12, 2019.

[19] "Reference standard atmospheres," *International Telecommunication Union*, vol. P.835-6, 2017.

[20] M. I. Skolnik, *Introduction to radar systems*, 2nd ed. New York: McGraw-Hill, 1980.

[21] R. J. Roy, M. Lebsock, L. Millán, R. Dengler, R. Rodriguez Monje, J. V. Siles, and K. B. Cooper, "Boundary-layer water vapor profiling using differential absorption radar," *Atmospheric Measurement Techniques*, vol. 11, no. 12, p. 6511–6523, Dec 2018.

[22] A. Battaglia and P. Kollias, "Evaluation of differential absorption radars in the 183 ghz band for profiling water vapour in ice clouds," *Atmospheric Measurement Techniques*, vol. 12, no. 6, p. 3335–3349, Jun 2019.

[23] R. J. Roy, M. Lebsock, and M. J. Kurowski, "Space-borne differential absorption radar water vapor retrieval capabilities in tropical and subtropical boundary layer cloud regimes," *Atmospheric Measurement Techniques*, vol. 14, no. 10, p. 6443–6468, Oct 2021.

[24] W. G. Read, Z. Shippony, and W. V. Snyder, "Microwave limb sounder (mls) forward model algorithm theoretical basis document," p. 248.

[25] L. Millán, R. Roy, and M. Lebsock, "Assessment of global total column water vapor sounding using a space-borne differential absorption radar," *Atmospheric Measurement Techniques*, vol. 13, no. 10, p. 5193–5205, Oct 2020.

[26] G. Maral, M. Bousquet, and Z. Sun, *Satellite communications systems: systems, techniques and technology*, 5th ed. Chichester, West Sussex, U.K: John Wiley, 2009.

[27] F. Depasse, M. Paesler, D. Courjon, and J. Vigoureux, "Huygens–fresnel principle in the near field," *Optics letters*, vol. 20, no. 3, pp. 234–236, 1995.

[28] D. Headland, Y. Monnai, D. Abbott, C. Fumeaux, and W. Withayachumnankul, "Tutorial: Terahertz beamforming, from concepts to realizations," *Apl Photonics*, vol. 3, no. 5, p. 051101, 2018.

[29] Y. Shen, X. Wang, Z. Xie, C. Min, X. Fu, Q. Liu, M. Gong, and X. Yuan, "Optical vortices 30 years on: Oam manipulation from topological charge to multiple singularities," *Light: Science & Applications*, vol. 8, no. 1, pp. 1–29, 2019.

[30] L. Zhang, H. Zhu, and X. Li, "A high gain oam antenna based on splitting spiral phase plate for c band," in *2017 Sixth Asia-Pacific Conference on Antennas and Propagation (APCAP)*. IEEE, 2017, pp. 1–3.

[31] H. Zhao, B. Quan, X. Wang, C. Gu, J. Li, and Y. Zhang, "Demonstration of orbital angular momentum multiplexing and demultiplexing based on a metasurface in the terahertz band," *ACS Photonics*, vol. 5, no. 5, pp. 1726–1732, 2017.

[32] Z. Zhang, S. Zheng, X. Jin, H. Chi, and X. Zhang, "Generation of plane spiral oam waves using traveling-wave circular slot antenna," *IEEE Antennas and Wireless Propagation Letters*, vol. 16, pp. 8–11, 2016.

[33] T. Yuan, Y. Cheng, H. Wang, and Y. Qin, "Mode characteristics of vortical radio wave generated by circular phased array: theoretical and experimental results," *IEEE Transactions on Antennas and Propagation*, vol. 65, no. 2, pp. 688–695, 2016.

[34] B. Liu, Y. Cui, and R. Li, "A broadband dual-polarized dual-oam-mode antenna array for oam communication," *IEEE Antennas and Wireless Propagation Letters*, vol. 16, pp. 744–747, 2016.

[35] G. Xie, Z. Zhao, Y. Yan, L. Li, Y. Ren, N. Ahmed, Y. Cao, A. J. Willner, C. Bao, Z. Wang *et al.*, "Demonstration of tunable steering and multiplexing of two 28 ghz data carrying orbital angular momentum beams using antenna array," *Scientific reports*, vol. 6, no. 1, pp. 1–9, 2016.

[36] R. Chen, H. Zhou, M. Moretti, X. Wang, and J. Li, "Orbital angular momentum waves: Generation, detection, and emerging applications," *IEEE Communications Surveys & Tutorials*, vol. 22, no. 2, pp. 840–868, 2019.

[37] J. Wang, J.-Y. Yang, I. M. Fazal, N. Ahmed, Y. Yan, H. Huang, Y. Ren, Y. Yue, S. Dolinar, M. Tur *et al.*, "Terabit free-space data transmission employing orbital angular momentum multiplexing," *Nature photonics*, vol. 6, no. 7, pp. 488–496, 2012.

[38] M. Oldoni, F. Spinello, E. Mari, G. Parisi, C. G. Someda, F. Tamburini, F. Romanato, R. A. Ravanelli, P. Coassini, and B. Thidé, "Space-division demultiplexing in orbital-angular-momentum-based mimo radio systems," *IEEE Transactions on Antennas and Propagation*, vol. 63, no. 10, pp. 4582–4587, 2015.

[39] W. Zhang, S. Zheng, X. Hui, R. Dong, X. Jin, H. Chi, and X. Zhang, "Mode division multiplexing communication using microwave orbital angular momentum: An experimental study," *IEEE Transactions on Wireless Communications*, vol. 16, no. 2, pp. 1308–1318, 2016.

[40] A. Trichili, C. Rosales-Guzmán, A. Dudley, B. Ndagano, A. B. Salem, M. Zghal, and A. Forbes, "Optical communication beyond orbital angular momentum," *Scientific reports*, vol. 6, no. 1, pp. 1–6, 2016.

[41] F. Zhu, S. Huang, W. Shao, J. Zhang, M. Chen,

W. Zhang, and J. Zeng, "Free-space optical communication link using perfect vortex beams carrying orbital angular momentum (oam)," *Optics Communications*, vol. 396, pp. 50–57, 2017.

[42] S. Yu, L. Li, G. Shi, C. Zhu, X. Zhou, and Y. Shi, "Design, fabrication, and measurement of reflective metasurface for orbital angular momentum vortex wave in radio frequency domain," *Applied Physics Letters*, vol. 108, no. 12, p. 121903, 2016.

[43] T. W. Crowe, W. L. Bishop, D. W. Porterfield, J. L. Hesler, and R. M. Weikle, "Opening the terahertz window with integrated diode circuits," *IEEE journal of solid-state circuits*, vol. 40, no. 10, pp. 2104–2110, 2005.

[44] J. V. Siles, K. B. Cooper, C. Lee, R. H. Lin, G. Chattopadhyay, and I. Mehdi, "A new generation of room-temperature frequency-multiplied sources with up to 10× higher output power in the 160-ghz–1.6-thz range," *IEEE Transactions on Terahertz Science and Technology*, vol. 8, no. 6, p. 596–604, Nov 2018.

[45] A. J. Alqaraghuli, A. Singh, and J. M. Jornet, "Novel cubesat combined antenna deployment and beam steering method using motorized rods for terahertz space networks," in *2021 IEEE Conference on Antenna Measurements & Applications (CAMA)*, 2021, pp. 560–561.

[46] M. Di Renzo, M. Debbah, D.-T. Phan-Huy, A. Zappone, M.-S. Alouini, C. Yuen, V. Sciancalepore, G. C. Alexandropoulos, J. Hoydis, H. Gacanin *et al.*, "Smart radio environments empowered by reconfigurable ai metasurfaces: An idea whose time has come," *EURASIP Journal on Wireless Communications and Networking*, vol. 2019, no. 1, pp. 1–20, 2019.

[47] G. Chattopadhyay, M. Alonso-delPino, C. Jung-Kubiak, T. Reck, C. Lee, N. Chahat, S. Rahiminejad, and D. González-Ovejero, "Terahertz antenna technologies for space science applications," in *2018 International Symposium on Antennas and Propagation (ISAP)*, 2018, pp. 1–2.

[48] M. Andersson, E. Berglind, and G. Björk, "Orbital angular momentum modes do not increase the channel capacity in communication links," *New Journal of Physics*, vol. 17, no. 4, p. 043040, 2015.

[49] K. B. Cooper, R. Rodriguez Monje, L. Millán, M. Lebsock, S. Tanelli, J. V. Siles, C. Lee, and A. Brown, "Atmospheric humidity sounding using differential absorption radar near 183 ghz," *IEEE Geoscience and Remote Sensing Letters*, vol. 15, no. 2, pp. 163–167, 2018.

BIOGRAPHY

Sergi Aliaga is a PhD student in the Ultra-Boradband Nanonetworking (UN) laboratory of the Electrical and Computer Engineering Department, under the Institute for the Wireless Internet of Things, at Northeastern University. He received two BSc in Telecommunications Engineering and Industrial Engineering from the Polytechnic University of Catalonia, under the CFIS (Interdisciplinary Higher Education Centre) program. Sergi carried out his Bacherlor Thesis at MIT on reconfiguration strategies for dynamic resource allocation algorithms in multibeam satellite systems. He gained industry experience through interning at SES Satellite and is the recipient of a fellowship from La Caixa foundation. His research interests include high data rate communications in the THz band, satellite communications, routing in satellite networks and system design for communications and sensing.

Ali Alqaraghuli is a PhD candidate in the Ultra-Boradband Nanonetworking (UN) laboratory of the Electrical and Computer Engineering Department at Northeastern University. He received his B.S. and M.S. degrees in Electrical Engineering form the University at Buffalo in 2018 and 2020, respectively. He gained industry experience through interning at Northrop Grumman Aerospace Systems and NASA Kennedy Space Center, and has lead the University at Buffalo Nanosatellite Laboratory as a communication systems lead engineer for RF and laser missions. He has served as an intern for the Submillimeter Wave Advance Technology group at the NASA Jet Propulsion Laboratory, as well in the Advanced Satcom Systems group at the MIT Lincoln Laboratory. His current research interests include high data rate space communications, mainly in the terahertz band.

Arjun Singh is an Assistant Professor in the Department of Engineering at the State University of New York Polytechnic Institute, Utica, NY. He obtained his Ph.D. in Electrical Engineering from Northeastern University, Boston, USA, under the guidance of Dr. Josep Jornet, as a member of the Ultra-Broadband Nanonetworking Laboratory, in December, 2021. His research interests include realizing Terahertz-band wireless communications, dynamic spectrum sharing, space networks, wavefront engineering, graphene-plasmonics and intelligent reflecting surfaces. In these areas, he has coauthored several publications in leading journals, as well as 1 US patent. He is a faculty mentor of the IEEE club at SUNY Polytechnic, a committee member for the STAR admissions committee and a reviewer for reputed journals including the IEEE communications magazine.

Josep M. Jornet (IEEE student member in 2008, member in 2013, senior member in 2020) is an Associate Professor in the Department of Electrical and Computer Engineering, the Director of the Ultrabroadband Nanonetworking Laboratory and a faculty member of the Institute for the Wireless Internet of Things and the SMART Center at Northeastern University. He received the B.S. in Telecommunication Engineering and the M.Sc. in Information and Communication Technologies from the Universitat Politecnica de Catalunya, Barcelona, Spain, in 2008, and received his Ph.D. from the Georgia Institute of Technology, Atlanta, GA, in 2013. Between 2013 and 2019, he was a faculty in the Department of Electrical and Computer Engineering at the University at Buffalo. His research expertise is in terahertz communications, wireless nano-bio-communication networks and the Internet of Nano-Things. In these areas, he has co-authored more than 200 peer-reviewed scientific publications, one book, and has also been granted

six US patents, which accumulate over 13,000 citations (h-index of 52) as of October 2022. He is serving as the lead PI on multiple grants from U.S. federal agencies including the National Science Foundation, the Air Force Office of Scientific Research and the Air Force Research Laboratory as well as industry. He is the recipient of multiple awards, including the 2017 IEEE ComSoc Young Professional Best Innovation Award, the 2017 ACM NanoCom Outstanding Milestone Award, the UB Exceptional Scholar Young Investigator Award in 2018 and Sustained Achievement Award in 2019, the NSF CAREER Award in 2019, the 2022 Martin W. Essigmann Excellence in Teaching Award, 2022 and the 2022 IEEE ComSoc RCC Early Achievement Award, among others. He has received multiple Best Paper Awards in multiple venues, including ACM NanoCom 2017, INFOCOM 2021 and the IEEE WoWMoM Non-Terrestrial Networks Workshop both in 2021 and 2022. He is a senior member of the IEEE and an IEEE Distinguished Lecturer (Class of 2022-2023). He is also the Editor in Chief of the Elsevier Nano Communication Networks journal and Editor for IEEE Transactions on Communications.